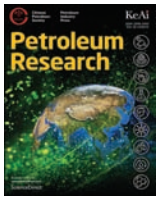
Petroleum Research 11 (2026) 730–742

Contents lists available at ScienceDirect

Petroleum Research

journal homepage: http://www.keaipublishing.com/en/journals/petroleum-research/



Full Length Article

Fluid flow mechanisms in tight gas reservoirs: A case study of Xujiahe formation in the central Sichuan basin



Jia Kang *, Gang Liu, Xin Kang, Peng Hu, Licai Qu

Exploration and Development Research Institute of PetroChina Daqing Oilfield Co. Ltd, Daqing, Heilongjiang, China

ARTICLE INFO

Article history:
Received 11 July 2025
Received in revised form
26 January 2026
Accepted 27 January 2026
Available online 2 February 2026

Keywords:
Tight sandstone gas reservoirs
High water content
Retrograde condensation
Stress sensitivity
Starting pressure
Xujiahe formation

ABSTRACT

Tight sandstone gas reservoirs exhibit low gas abundance and extensive gas-bearing lithology, presenting promising prospects for future exploration and development. However, their exploitation in the Sichuan Basin is severely constrained by low recovery efficiency, high water saturation, and pronounced retrograde condensation phenomena. In this study, we aim to analyze the complex fluid flow behavior within these reservoirs to overcome these challenges. To achieve this, a comprehensive experimental program is utilized, encompassing nuclear magnetic resonance, micro-computed tomography, core flooding, and retrograde condensation tests. The analysis reveals that tight sandstone reservoirs feature low porosity, low permeability, and poor pore connectivity, with pore structures predominantly composed of nanometer-to 10-μm-size micropores. Pore size distributions in both Type I and Type II reservoirs exhibit multimodal characteristics, rendering them highly sensitive to stress changes and condensate-induced formation damage. Permeability demonstrates significant hysteresis effects during cyclic changes in confining pressure. Precisely, after two complete cycles of increasing and decreasing confining pressure, average permeability damage rates reach 52.08% and 46.1%, respectively. This indicates damage levels ranging from moderate-weak to moderate-strong. In contrast, variations in pore pressure exhibit minimal impact on permeability. Under irreducible water saturation conditions, the average gas phase damage rate is 64%. Furthermore, initiating fluid flow within the reservoir requires a specific threshold pressure. The average damage rate caused by retrograde condensation is 24.7%. This experimental investigation elucidates the reservoir's pore-throat characteristics, the dynamics governing gas-water and gas-oil flow, and the damage patterns associated with retrograde condensation. These insights provide critical foundational data for optimizing development strategies and designing effective stimulation measures to achieve enhanced recovery.

© 2026 Chinese Petroleum Society. Publishing services by Elsevier B.V. on behalf of KeAi Communications Co. Ltd. This is an open access article under the CC BY-NC-ND license (http://creativecommons.org/licenses/by-nc-nd/4.0/).

1. Introduction

Tight sandstone gas reservoirs exhibit low abundance and extensive gas-bearing lithology, presenting broad prospects for exploration and development. However, the current production in the Sichuan Basin is declining due to tight reservoir rock, low porosity and permeability, high water content, and severe retrograde condensation, which greatly constrain the development and production of the gas field. The gas reservoir has the following key development characteristics (Gao et al., 2025; Jiang et al., 2023): (1) Low natural production capacity: In general, gas wells require hydraulic fracturing to achieve industrial production rates. (2) Low overall production: The wells exhibit low cumulative gas production and recoverable reserves. (3) Low production and recovery rates: The gas production rate is typically less than 3%, and the recovery rate is below 30%. (4) Short stable production period: Production of gas wells declines rapidly initially (by 20%–40%) but tends to stabilize later. The stable production period is typically less than 3 years, with the field's stable output maintained by well interspacing. (5) Long production cycle: There is a prolonged period of low production and low-pressure extraction, often exceeding 30 years.

The high water content and retrograde condensation features of the gas reservoir lead to the following: (1) Increased start-up pressure gradient: High bound water saturation occupies

* Corresponding author. Exploration and Development Research Institute of PetroChina Daqing Oilfield Co. Ltd., China.
E-mail address: kangjia@petrochina.com.cn (J. Kang).
Peer review under the responsibility of Editorial Office of Petroleum Research.

https://doi.org/10.1016/j.ptlrs.2026.01.018
2096-2495/© 2026 Chinese Petroleum Society. Publishing services by Elsevier B.V. on behalf of KeAi Communications Co. Ltd. This is an open access article under the CC BY-NC-ND license (http://creativecommons.org/licenses/by-nc-nd/4.0/).

effective seepage channels, increasing the resistance to gas flow and necessitating a higher start-up pressure gradient for extraction, resulting in additional energy consumption during the extraction process. (2) Exacerbated permeability reduction: The presence of reservoir water amplifies the rock's stress sensitivity, meaning that as pore pressure drops during production, the effective stress on the rock increases, causing pore throats to constrict and exacerbate the reduction of gas phase permeability. (3) Gas trapping and cut-off: Pore water can flow along high-permeability pathways, driven by capillary forces (spontaneous imbibition) into smaller pores, which can trap and cut off gas in the pores, a phenomenon known as the Jamin effect or water-lock effect. (4) Wellbore liquid accumulation: Increased water saturation leads to problems such as water breakthrough and wellbore liquid loading, which impedes efficient gas production and can lead to a significant drop in productivity (Huang et al., 2023; Zhao et al., 2021). (5) Condensate blockage: When reservoir pressure falls below the dew point, retrograde condensation occurs within the gas reservoir, causing the gradual formation of condensate oil. The accumulating liquid increases flow resistance during the extraction process and can plug small pores, thereby hindering production (Tran et al., 2024).

Behrang et al. (2016) and Liu et al. (2023a, b) separately evaluated the impact of retrograde condensation in tight water-bearing condensate gas reservoirs. While Behrang et al. (2016) focused on a retrograde condensation damage evaluation experiment, Liu et al. (2023a, b) performed a recovery factor evaluation experiment. Their combined findings indicated that the presence of condensate oil increases gas phase flow resistance and reduces the degree of gas utilization. Simultaneously, higher condensate oil content and pressure lead to greater damage caused by retrograde condensation. Therefore, in the early stages of development of such gas reservoirs, the production pressure difference should be reduced as much as possible (Zhang et al., 2023, 2025).

Many researchers combined digital and physical model methods to investigate the seepage characteristics and the anti-condensate damage in tight sandstone reservoirs (Kang et al., 2022, 2023). Their findings suggested that for unfractured vertical wells in the late development stage, the damage from water locking and anti-condensate effects can be substantial, potentially amounting to 80%, and that fracturing can significantly mitigate the damage from both phenomena (Ajagbe et al., 2020; Huang et al., 2022; Mohamadi-Baghmolaei et al., 2021; Zhang et al., 2020). Observations from the Great Green tight gas reservoir illustrate this damage clearly. A typical gas well in this field initially had an unobstructed flow rate of 66 $\times$ 10^4 m^3/d. After condensation occurred, the unobstructed flow rate dropped from 23.2 $\times$ 10^4 m^3/d to 15.6 $\times$ 10^4 m^3/d, an average decrease of 32.8% (Fig. 1a). The damage to the formation caused by condensate recondensation is relatively significant. The gas phase relative permeability decreases sharply as formation pressure drops and the water-gas ratio increases (Fig. 1b). For instance, when the formation pressure decreases from 35 MPa to 25 MPa, and the production water-gas ratio increases from 1.0 $m^3/10^4$ m^3–2.8 $m^3/10^4$ m^3, the gas phase relative permeability decreases by 70%. This indicates that once the formation water production exceeds its saturation condensate water content—that is, after the invasion of liquid water into the formation, the productivity of the gas reservoir will rapidly decrease (Zahedizadeh et al., 2022, 2022, 2022).

Numerous studies have shown that water locking and retrograde condensation damage can significantly reduce core permeability, which in turn diminishes reservoir production (Kamel et al., 2022; Li, 2022, 2023). As highlighted earlier, the target study area is characterized by high water content, rapid production decline, retrograde condensation issues, and low recovery rates, which severely impede gas field development. Through this experimental research, we aim to better understand the target reservoir's pore throat characteristics, the dynamics of gas-water and gas-oil seepage laws, and effective anti-condensate pollution measures. This foundational knowledge can provide a solid basis for adjusting current development plans, implementing production stimulation, and transforming operational measures. It can also offer oil and gas developers a more comprehensive and in-depth understanding of the tight sandstones in the Sichuan Basin, as well as a thorough grasp of the pore and seepage/flow characteristics of similar reservoirs, to guide practical oil and gas production strategies.

2. Geological setting

The target reservoir is located in the southern part of a gently sloping structural belt within the central Sichuan Basin. It represents a transition zone between the gentle structural area of the ancient Sichuan uplift and the high, steep structural area of southeastern Sichuan. The general structural trend of the ground is a large slope, or monocline, dipping consistently from the southeast toward the northwest. The Lower Permian strata follow this pattern, forming a monoclinic structure that dips in the same direction. Against this large regional slope, a series of smaller, local structural traps has developed, oriented mainly from south to north. The Xujiahe Formation is a thick sequence—ranging from 500 to 600 m—composed of continental source clastic rock that was deposited in alternating inland river and lake sediments. The primary reservoir intervals are found within the second member of the Xujiahe Formation. It is mainly composed of gray, medium-grained to medium-fine-grained lithic feldspar sandstone, lithic feldspar sandstone, and lithic quartz sandstone, which hold the key deposits (Fig. 2).

3. Pore throat characteristics

Reservoir pore throat characteristics define both how much fluid a reservoir can store (storage characteristics) and how easily

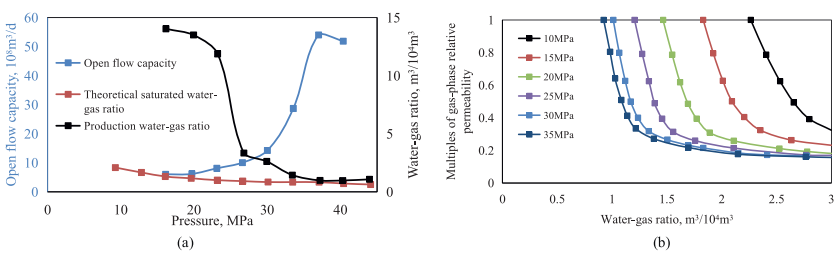


Fig. 1. Influence of gas-water ratio on gas phase relative permeability. (a) Variation of absolute open flow with pressure (b) Relationship between gas phase relative permeability and different formation pressures and different production water-gas ratios.

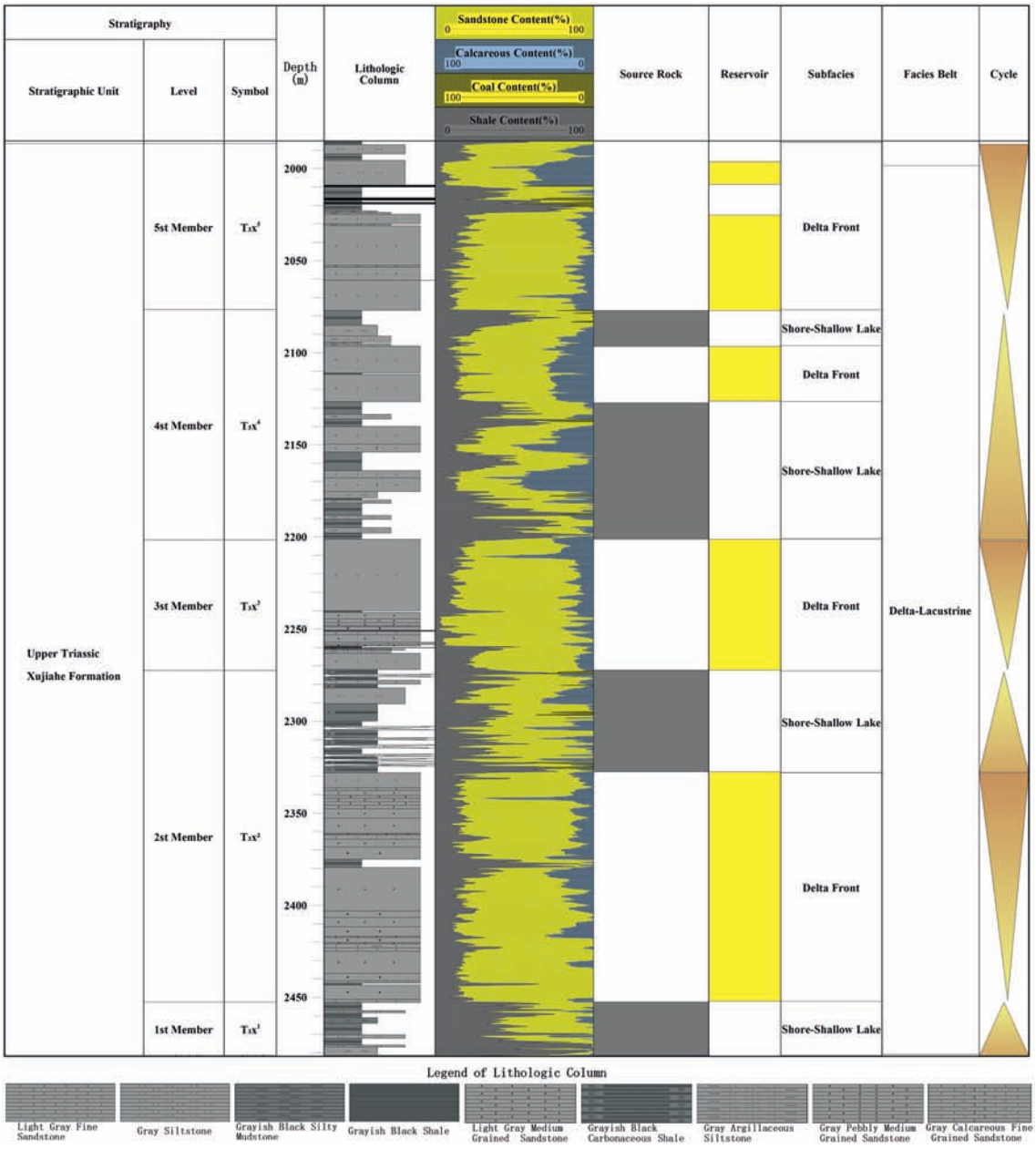


Fig. 2. Comprehensive reservoir columnar diagram of the study area.

that fluid can move through the rock (seepage characteristics). Understanding these characteristics is fundamental for evaluating the reservoir's physical properties and is crucial for planning production stimulation and transformation operations.

3.1. Analysis of cast thin sections

The reservoir in Member 2 of Xujiahe Formation is primarily composed of superimposed underwater distributary channel sand bodies, ranging in thickness from 70 to 100 m, and exhibits strong rock heterogeneity. The dominant rock types are fine-to medium-grained feldspar lithic sandstone and lithic feldspathic sandstone, with a small amount of lithic quartz sandstone. The composition breakdown is typically quartz (50%–78%), feldspar (6%–16% potassium feldspar, followed by 1%–2% plagioclase), and debris (14%–22%, primarily sedimentary and metamorphic rock fragments). Interstitial material is mainly argillaceous mica, with some calcite cementation (Fig. 3). Based on data collection and observation of thin sections, the predominant pore types are residual primary intergranular pores, intergranular dissolved pores, and intragranular dissolved pores. Mold pores are also present, with occasional miscellaneous pores and micro-fractures (Fig. 3). The reservoir quality metrics are as follows: effective porosity (7.56%–12.39%), low permeability (0.135–6.09 mD, with an average value of 0.388 mD), and high water saturation (32.50%–61.65%).

3.2. Rock nuclear magnetic resonance (NMR) analysis

The present study uses the principle of NMR to analyze rock properties. First, the relaxation time of pore fluids is measured and

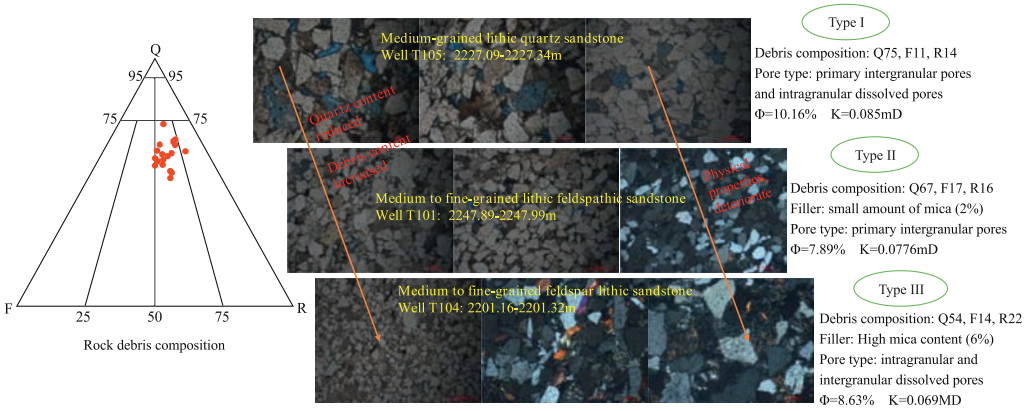


Fig. 3. Reservoir characteristics of Member 2 of Xujiahe Formation in the central Sichuan Basin.

calculated. Then, a calibration relationship is established using standard samples to determine the rock's porosity and pore size distribution. We used the MRCoresHP20L NMR analyzer for this experiment. To obtain the T2 cutoff value and nuclear magnetic porosity, we measured the T2 spectra of core samples in two states: dry and vacuum/pressurized water-saturated. Fig. 4 shows the one-dimensional NMR T2 spectra obtained from these two samples.

The T2 spectrum of the water-saturated rock samples primarily shows a bimodal distribution, indicating the development of both small and large pores and strong heterogeneity. The two spectral peaks are distributed within the 1–20 ms and 20–1000 ms ranges, respectively. Based on these distributions, the samples were categorized into three reservoir types: Class I reservoir rocks, Type II reservoir rocks, and Type III reservoir rocks. Regarding Class I reservoir rocks, sample T101-1(19–53) exhibits a similar proportion of small and large pores, and sample T107-4(22–37) is dominated by larger macropores. Regarding Type II reservoir rocks, sample T107-3(9–55) has a relatively large proportion of small pores compared to large ones. Regarding Type III reservoir rocks, sample T110-66 shows a single-peak distribution, with spectrum peaks concentrated mainly between 1 and 20 ms. The pores are predominantly small. To verify the reliability of the nuclear magnetic porosity measurements and further analyze the rock pore size distribution characteristics, supplementary tests were conducted. These include the alcohol method porosity test and the saturated water weighing porosity method. The porosity results derived from the saturated water nuclear magnetic experiment demonstrated the best correlation with the results from the alcohol method (Table 1).

A comparison of the nuclear magnetic porosity and the alcohol method porosity reveals a systematic relationship dependent on pore size distribution. First, when small pores (relaxation time 1–20 ms) are dominant (i.e., they constitute a larger proportion of total pores), the nuclear magnetic porosity is greater than the alcohol method porosity. Second, when the proportion of small pores (1–20 ms) and larger pores (20–1000 ms) is similar, the nuclear magnetic porosity is close to the alcohol method porosity. Third, when larger pores (20–1000 ms) are dominant (i.e., they are more developed and constitute a larger proportion), the nuclear magnetic porosity is smaller than the alcohol method porosity. These differences stem from method-specific detection errors; the injection (alcohol) method has a detection blind zone for small pores, while the NMR method has a detection loss error for large pores (Fig. 5).

The nuclear magnetic T2 spectrum relaxation time and pore size are converted using an empirical coefficient for tight sandstone reservoirs. In both magnetic fields, the T2 cutoff value is generally greater than 3000 ms, and the overall transverse relaxation time T2 is as follows:

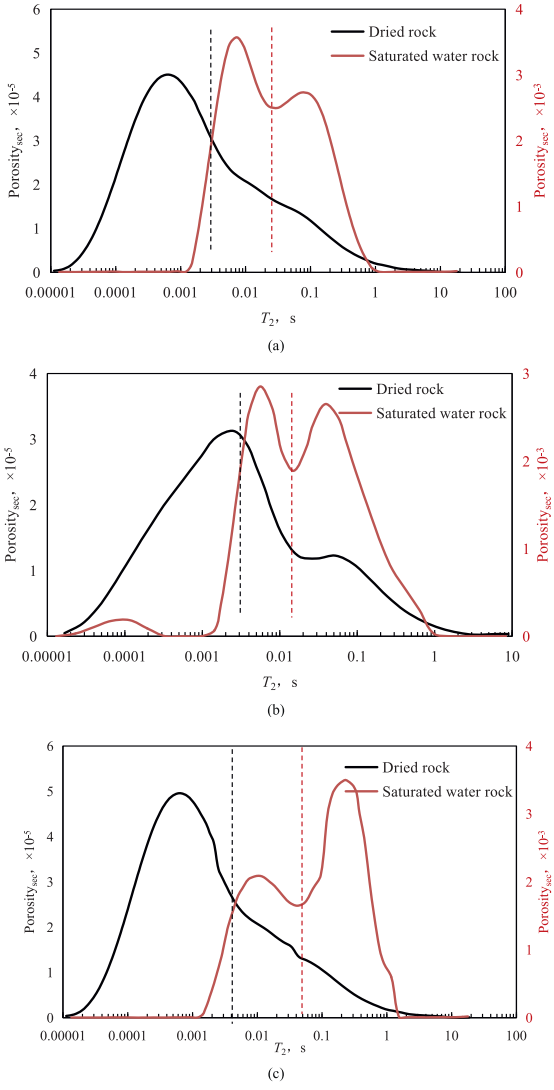


Fig. 4. NMR T2 spectrum. (a) Sample T107-3(9/55); (b) Sample T101-1(19/53); (c) Sample T107-4(22–37).

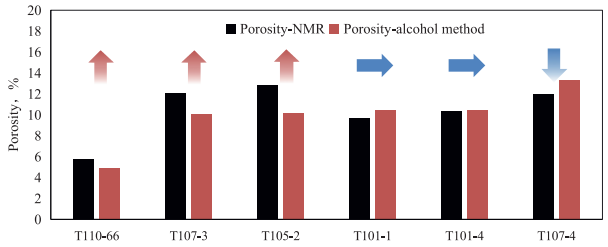


Fig. 5. Comparison between nuclear magnetic porosity and alcohol method porosity.

$$T_2 = \frac{r}{\rho_2 F_s} \Rightarrow r = CT_2 \quad (1)$$

Where ρ_2 is the transverse surface relaxation rate (μm/ms); r is the pore throat radius (μm); and F_s is the shape factor. The target area is a tight sandstone reservoir. Using the empirical coefficient C for this reservoir type, which is 20 nm/ms, the pore size is calculated to obtain the pore size distribution of each rock in the target well (Fig. 6).

The nuclear magnetic pore size distribution reveals distinct characteristics among the samples, indicating high heterogeneity across the reservoir. T110-66 is dominated by a single peak, with 62% of its pores mainly distributed between 20 and 400 nm (62%), and very few pores larger than 1 μm; it is classified as a Type III reservoir. T107-4(22–37) is dominated by large pores, with a pore radius of 400 nm–10 μm; it is classified as a Type I reservoir. T101-4(29–68) has a relatively large proportion of small pores, with a pore radius of 20–400 nm; it is classified as a Type II reservoir. Across the Type I and II reservoir rocks, pores ranging from 200 to 400 μm account for 32.8%–62.4% of the total pores, and larger pores ranging from 400 to 10000 μm account for 22%–41% of the total pores. This variability in pore size distribution among the samples indicates that the reservoir is highly heterogeneous.

While the influence of pore size distribution on pore connectivity is not absolute, a significant correlation often exists. Digital rock physics technology facilitates an intuitive understanding of this correlation (Fig. 7). In cores with a high proportion of small pores, the pore structure is complex, characterized by short and narrow throats. This leads to high fluid seepage resistance and a tendency for liquid locking during oil and gas production and stimulation operations, which can block the reservoir. In such cases, the design of production strategies and stimulation measures profoundly impacts production effectiveness. Particularly, large-scale acid fracturing paired with low-friction fracturing fluids is crucial for enhancing production in these reservoirs. Conversely, cores with a high proportion of large pores have a relatively simple pore structure with larger pores and throats, resulting in low fluid seepage resistance and favorable oil and gas production outcomes. Stimulation treatments for these reservoirs focus more on acidizing or fracturing, and the required scale of fracturing is considerably smaller than that for reservoirs dominated by small pores. Research on pore size distribution is, therefore, essential for formulating and optimizing appropriate production strategies and stimulation measures for different reservoir types.

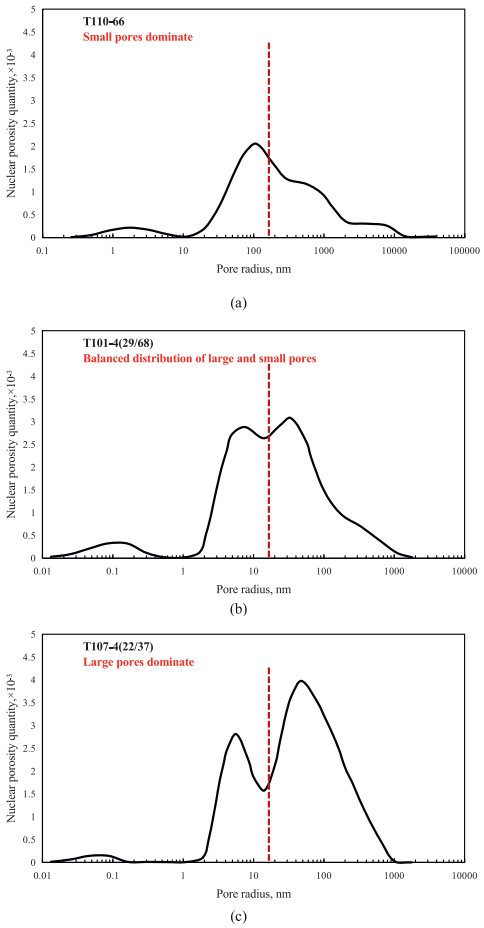


Fig. 6. NMR test pore size distribution. (a) Rock with small pore dominance; (b) rock with balanced small and large pore distribution; (c) rock with large pore dominance.

3.3. X-ray computed tomography (CT) analysis

X-ray CT scanning is a non-destructive, non-invasive three-dimensional imaging technology. In recent years, it has been increasingly used for studying the three-dimensional pore structure of porous media. The resulting three-dimensional digital rock images accurately reflect the internal microstructure of the rock. By applying specific image processing methods (Fig. 8), researchers can quantify the characteristics of the rock's internal pore space, offering a valuable alternative approach for specialized rock analysis (Sadegh et al., 2019; Kalam et al., 2019). After X-ray CT scanning, the three-dimensional pore structure of the rock is reconstructed using the filtered back-projection method. Noise elimination is then performed to improve the accuracy of subsequent pore identification. Finally, the rock pores are segmented using the threshold segmentation method, followed by an analysis of pore connectivity. Some representative results from both segmentation and connectivity analyses are shown in Table 2.

Table 1
Comparison of data from three porosity measurement methods.

Sample	T101-1(19/53)	T101-4(29/68)	T110-66	T107-3(9/55)	T107-4(22/37)	T105-2(12/57)
Saturated water nuclear magnetic porosity (%)	9.668	10.369	5.699	12.056	11.973	12.812
Saturated water weighing porosity (%)	8.929	9.845	4.545	11.535	11.510	11.938
Alcohol method porosity (%)	8.448	9.291	4.902	10.923	10.650	11.905

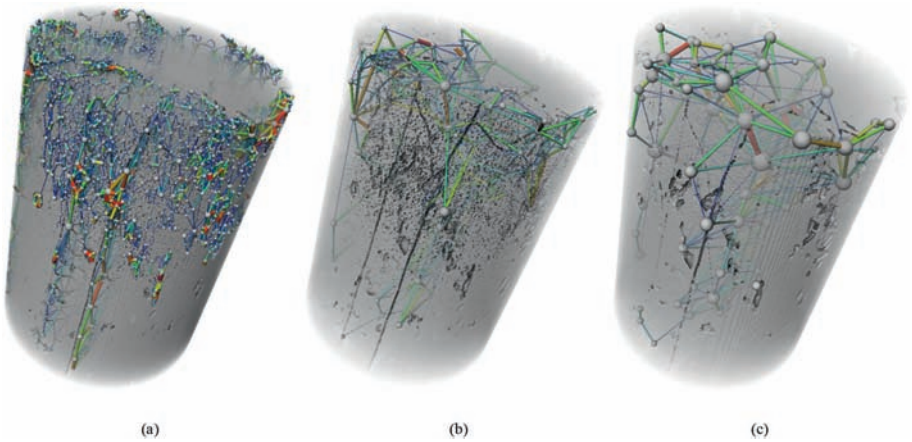


Fig. 7. Pore size distribution in three types of rock samples. (a) Rock with predominantly large pores; (b) rock with comparable proportions of large and small pores; (c) rock with predominantly small pores.

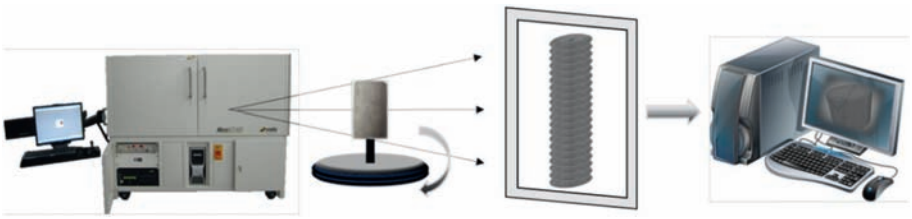


Fig. 8. X-ray CT scanning proces.

Overall, the rock sample exhibits a tortuosity range of 9.33–23.29 and a fractal dimension of 1.51–2.01. The pore structure is characterized by few, small, and weakly connected pores, which indicates low porosity and, consequently, low permeability. The pore size distribution was then statistically calculated, and the results are shown in Fig. 9. The micron pore size distribution range of the sandstone in the Xu-2 Member is 62–200 μm, and the porosity determined via micron CT analysis shows a good correlation with the porosity measured by the gas expansion method (Fig. 10). However, some sample properties vary. For instance, Well T110 displays the poorest physical properties; its pore size range is concentrated within 50–150 μm, the pore structure is complex, and the tortuosity is high, at 23.29. These findings are consistent with the nuclear magnetic test results. The micron CT resolution is

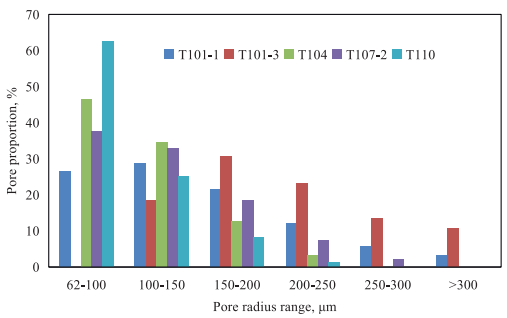


Fig. 9. Pore size distribution range of each rock.

Table 2
Rock pore segmentation and connectivity analysis results.

Rock sample	Tortuosity	Fractal dimension	T101-1 pore structure	T101-1 pore connectivity
T101-1	9.33	1.90		
T110	23.29	1.51		
T104	14.78	1.84		
T101-3	6.90	2.01	The blue part indicates pores	The red part indicates the area with larger pores The green part indicates the area with smaller pores

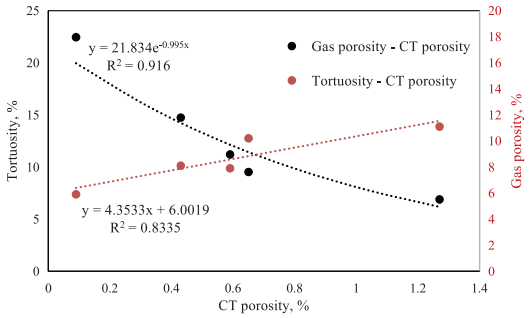


Fig. 10. Relationship between CT porosity, tortuosity, and gas porosity.

26.53 μm, and the corresponding test porosity derived from this method is generally less than 1%, which is 1–2 orders of magnitude lower than the results obtained using the gas method. This indicates that macropores larger than 60 μm do not contribute much to the total reservoir space. There is a strong negative correlation between macropore space tortuosity and overall porosity: the higher the porosity, the better the pore throat connectivity.

Using water for seepage simulation can not only study the connectivity of pores but also study the flow channels of rocks. As shown in Fig. 11, the water flow velocity distribution highlights fractures as the main flow channels in this type of core, which connect previously isolated pores. Matrix pores, by contrast, primarily serve as gas storage spaces, which is the fundamental reason for the low permeability of rocks. Based on the collection and arrangement of petrological, pore throat, and physical property characteristics, the reservoir types are divided into three categories (Table 3).

4. Fluid seepage characteristics

Mastering the seepage rules between gas, water and gas, and oil is crucial for optimizing and adjusting gas field development strategies to increase oil and gas production. The characteristics of this fluid seepage are typically analyzed through experiments such as gas-water relative permeability test, starting pressure gradient test, confining pressure 2-L-two-drop permeability test, and condensate oil pollution test.

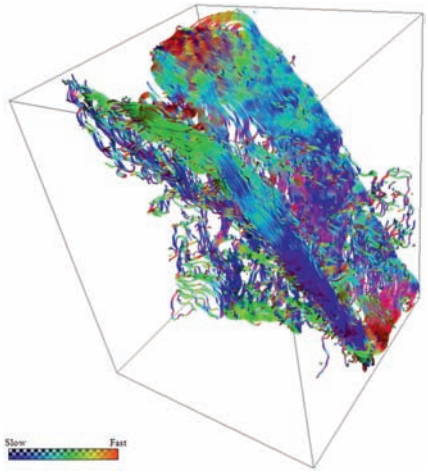


Fig. 11. Distribution of water velocity in rocks.

4.1. Full-diameter rock water drive gas relative permeability test

The full-diameter rock water drive gas relative permeability curve test is performed to determine the impact of the complex pore structure of tight gas reservoirs on the two-phase water and gas seepage capacity. This clarification is vital for accurately determining and evaluating gas reservoir productivity. The relative permeability curve is measured using a fully automatic unsteady-state gas-water relative permeability curve measuring instrument, following the unsteady-state method. The process involves a constant pressure difference displacement experiment where the inlet and outlet flow rates, pressure differences, and time are recorded. The relative permeability curve is then obtained through automatic history matching, and the relationship between permeability and maximum gas phase permeability is summarized (Figs. 12 and 13).

The co-permeability range of the sample is 41.43%–56.13%. The irreducible water saturation is high, ranging from 32%–41%, and the endpoint permeability is low, at 0.1–0.32 mD. These properties indicate a low-permeability rock sample with small, poorly connected pores. The initial water saturation is also relatively high, at 32%. The isotonic point of the gas and water phases is 60%, and the isotonic permeability is 0.01–0.05 mD. This indicates that the pore throat structure is complex, the pore throat size is small, and permeability is highest in the gas phase. The point relative permeability exhibits a high degree of correlation.

4.2. Determining the starting pressure gradient of gas in full-diameter rock with bound water

This is performed to quantify the resistance that must be overcome for gas flow (seepage) when an adsorption or hydration film (irreducible water) lines the rock surface. This resistance varies based on rock permeability as well as the irreducible water saturation conditions. The findings will provide guidance for optimizing water injection parameters during field development, such as well spacing, flow rate, and pressure differential. The experiment was conducted under an induced irreducible water environment created by re-centrifuging saturated rock samples. The starting pressure gradient was determined using the following steps: (1) the gas flow rate through the rock sample was gradually decreased, (2) the pressure difference at both ends of the rock was measured at each flow rate, (3) the flow-pressure gradient experimental curve was plotted from the collected data, and (4) a fitting curve was extrapolated to find the intercept on the pressure gradient axis. This intercept represents the “starting pressure,” and the starting pressure was divided by the length of the rock sample to calculate the “starting pressure gradient.” The results of the starting pressure test are shown in Figs. 14 and 15.

The gas-phase starting pressure gradient under irreducible water conditions is jointly affected by the rock sample's permeability and its irreducible water saturation, and permeability and irreducible water saturation exhibit a strong negative correlation. The average damage rate of bound water to gas phase permeability is 64%. The calculation formula is detailed in Formula 2. The threshold pressure gradient of Type III reservoirs (0.275–0.279 MPa/cm) is significantly higher than that of Type II reservoirs (0.225–0.232 MPa/cm). The better the porosity and permeability conditions, the lower the threshold pressure gradient. In terms of production recommendations for research block based on gas test production results, a reasonable well spacing is 500~1000 m, the average pressure in the middle of the reservoir is approximately 30 MPa, and the bottom hole flowing pressure is approximately 10 MPa.

Table 3
Reservoir type classification.

Reservoir	Physical property parameters				Pore characteristic parameters			
	Porosity %	Permeability mD	Average porosity %	Average permeability mD	Displacement pressure MPa	Median pressure MPa	Maximum pore radius μm	Median radius μm
Type I	≥10	≥0.2	12.5	0.6	<1.2	<7	>0.6	>0.1
Type II	8–10	0.08–0.2	8.11	0.05	0.7–1.8	6–12	0.4–1	0.07–0.15
Type III	4–8	0.05–0.1	6.71	0.02	1–3	8–16	0.2–0.6	0.04–0.1

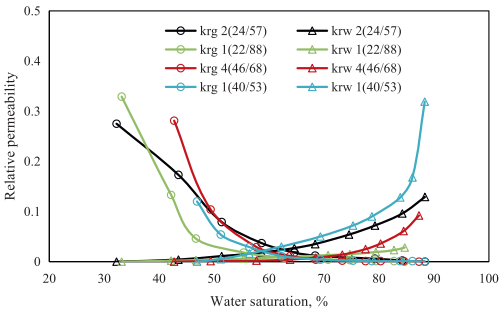


Fig. 12. Relative permeability curve.

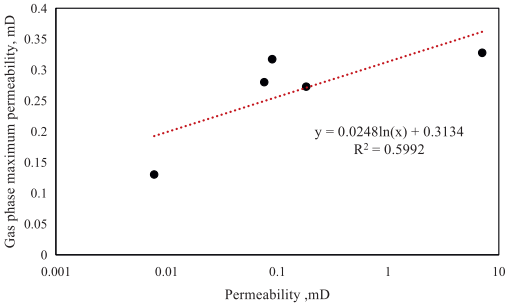


Fig. 13. Relationship between permeability and maximum gas phase permeability.

$$\overline{\varphi_{per}} = \left[\sum_{i=1}^{n} (K_{si} - K)/K\right] \Big/ n \quad (2)$$

Where $\overline{\varphi_{per}}$ is the average damage rate of bound water to gas phase permeability (%); n is the number of experiments in the same group; K is the permeability of samples after drying (mD); and K_{si} is the rock permeability under different bound water conditions (mD).

4.3. Two-round stress sensitivity analysis under varying confining pressure

The experimental setup was designed to replicate actual reservoir dynamics. A constant internal pressure was applied while cyclically increasing and decreasing the confining pressure twice, simulating the complete cycle of reservoir formation and exploitation. The changes in full-diameter rock permeability, porosity, and pore volume compressibility coefficient were monitored during and after the entire process. The experimental results are shown in Fig. 16.

When the internal pressure remains constant, an increase in confining pressure causes the rock sample's permeability to decrease first rapidly, then slowly. The effective stress range of 10~12 MPa acts as a key dividing point for this behavior. Across the four processes (two instances of increasing and two of decreasing pressure), plastic damage is induced in the reservoir, resulting in a lag in permeability recovery. The resulting permeability reduction curve shows two different stages, each characterized by a different slope. In the first stage (rapid decrease), the reservoir rock sample is compressed, and initial deformation occurs in the larger pores, easy-to-close throats, and micro-fractures. The closure of these significant spaces results in a sharp, rapid decline in overall permeability. In the second stage (slow decrease), after the effective stress reaches the 10–12 MPa threshold, the more resistant, smaller pores and difficult-to-close throats undergo deformation. The overall compression rate of the rock sample diminishes, causing the permeability to decrease gradually until it nearly stagnates. Based on these mechanical responses, the tested reservoirs (Type II, Type III, and Type III) can be categorized into three types: (1) relatively high porosity and permeability-sensitive reservoirs; (2) tight, low-sensitive reservoirs; and (3) fracture-containing, highly sensitive reservoirs. Relatively high porosity and permeability-sensitive reservoirs feature well-developed intragranular dissolved pores, intergranular dissolved pores, and primary intergranular pores. They are highly sensitive to loading confining pressure. Tight, low-sensitive reservoirs are characterized by compacted particles, a high cementation degree, and

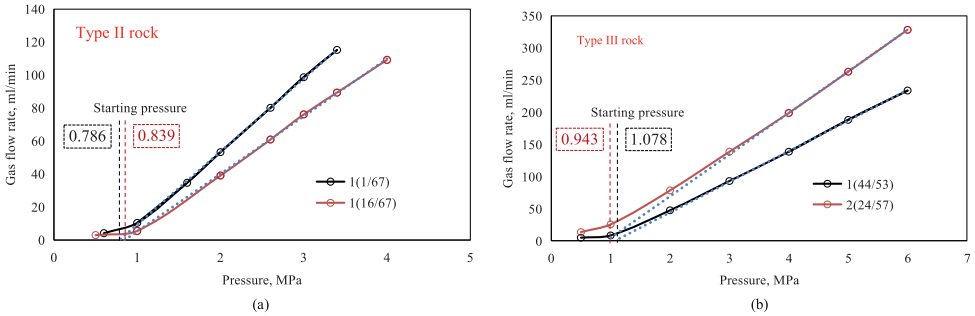


Fig. 14. Gas flow rate and pressure relationship curve. (a) Type II rock; (b) Type III rock.

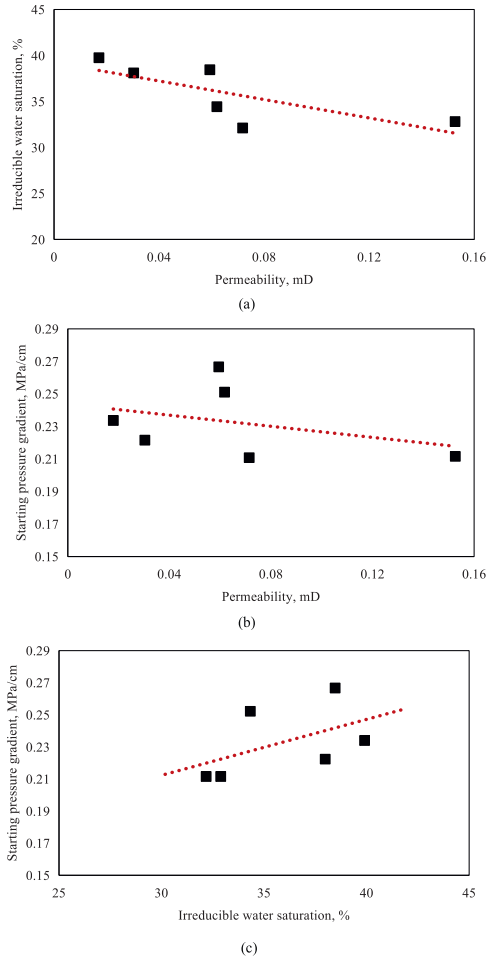


Fig. 15. Relationship between irreducible water saturation, starting pressure gradient, and permeability. (a) Relationship between irreducible water saturation and permeability; (b) Relationship between starting pressure gradient and permeability; (c) Relationship between irreducible water saturation and starting pressure gradient.

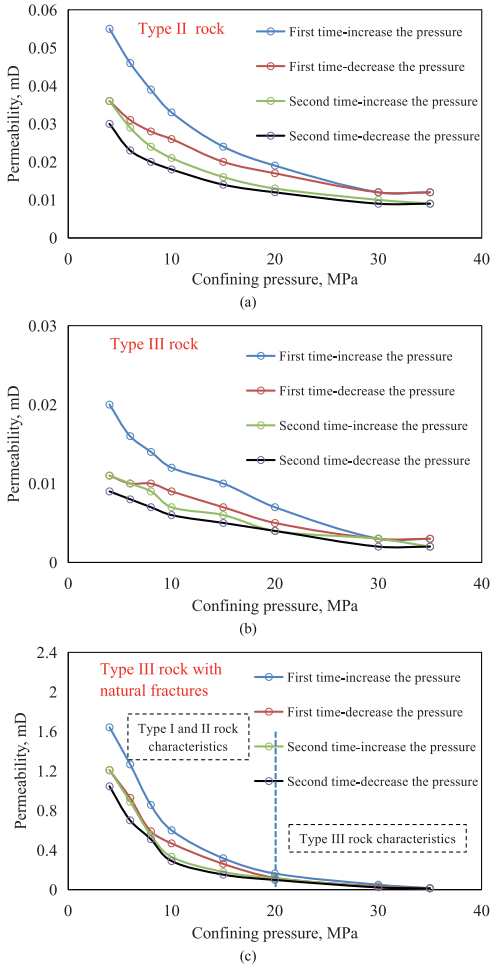


Fig. 16. Permeability variations with increasing confining pressure. (a) Sample T105-2(12/57); (b) Sample T104-3(3/63); (c) Sample T110-2(1/55).

development of only residual intergranular and intragranular dissolved pores. These exhibit weak sensitivity to loading confining pressure. The rock particles in fracture-containing, highly sensitive reservoirs are severely fractured and prone to breaking and penetration under low-pressure loading. In a relatively high permeability state, the permeability rapidly decreases as the confining pressure increases. When the pressure exceeds 15 MPa, the fractures close, leading to a significant shift in the permeability change rate. For high porosity and permeability-sensitive reservoirs, the initial permeability change rate is approximately 20%, and the final change rate is approximately 40%, with the curve flattening significantly at pressures exceeding 20 MPa. For tight, low-sensitive reservoirs, the initial permeability change rate is approximately 10%, and the final change rate is approximately 20%, which tends to flatten out at pressures greater than 15 MPa. The variation in the change rate among samples during the second pressure cycle (increasing and decreasing) is less pronounced compared to the first cycle. Plastic damage primarily occurs in the first loading process (Fig. 17).

4.4. Two-round stress sensitivity analysis under varying internal pressure

The experimental setup was designed to replicate the actual reservoir dynamics. A constant confining pressure was applied, and changes in formation pressure during the two key phases—reservoir formation and reservoir exploitation—were simulated by cycling the internal pressure twice (increasing and decreasing). The process involved two distinct cycles. In the first pressure cycle, the internal pressure was gradually decreased according to a set gradient while the confining pressure remained fixed at a value representative of the formation pressure. The second pressure cycle followed the same methodology of the variable internal pressure and constant confining pressure permeability stress sensitivity experiment. This stage aimed to simulate the stress-sensitive permeability characteristics during the actual production and storage of oil. The experiment measured the changes in the full-diameter rock permeability throughout both rounds of pressure cycling (increase and decrease) and after the test concluded. The experimental results are shown in Fig. 18.

In the first pressure increase, when the internal pressure reached 25 MPa, the permeability increased by 3.27–15.1 times (average 11.15). The multiplier exhibited a slight increasing tendency as the permeability increased. During the subsequent pressure reduction, when the internal pressure dropped to 1 MPa, the permeability retention was relatively stable, remaining at a level of 31.9%–94.17% (average 78.13%).

In the second pressure increase, when the internal pressure reached 25 MPa, the permeability increased by 7.26–15.16 times (average 9.59), which was 1.56 times less than the first increase. As the permeability increased, the increase factor tended to rise. After

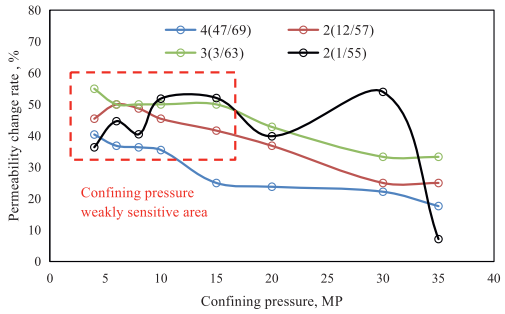


Fig. 17. Permeability change rate after two cycles of increasing and decreasing confining pressure.

the subsequent pressure reduction, when the internal pressure dropped to 1 MPa, the permeability maintenance level was 27.16–81.04% (average 53.9%). The permeability loss rate was moderately weak and had no obvious correlation with the permeability value itself. The greater the porosity and the more developed natural fractures, the stronger the hysteresis phenomenon of permeability reduction. Furthermore, internal pressure has a weak effect on permeability in Type I and Type II reservoirs when the pressure is greater than 15 MPa. For Type III reservoirs, this weak effect occurs when the pressure is greater than 12 MPa.

4.5. Condensate oil contamination experiment near the wellbore zone

During the production of a condensate gas reservoir, the reservoir pressure continuously decreases. When the pressure drops below the dew point pressure, condensate oil gradually forms. This condensate oil increases flow resistance and changes the fluid dynamics in or near the wellbore from a one-way flow to a gas-oil two-phase flow, which severely impacts the production capacity of the gas reservoir. The experiment was designed to reflect the relationship between the reduction of formation pressure and the degree of damage caused by condensate oil, providing data for productivity prediction and formation pressure maintenance strategies. This was achieved by testing the ability of natural gas with varying oil saturations to flow through rock samples. As the pressure within the rock decreases, retrograde condensation occurs, and the continuous precipitation of condensate oil leads to a decrease in gas phase permeability. The results showed a direct correlation between pressure drop and permeability damage: when the formation pressure decreased to 25 MPa, the gas phase permeability damage rate was 6.23%–13.78% (average 9.6%), and when the formation pressure decreased to 5 MPa, the damage rate was 19.85%–29.10% (average 24.7%) (Figs. 19 and 20).

In the retrograde condensation experiment, the decrease in the rock's internal pressure causes the production of condensate oil and results in damage to the gas phase permeability. While the extent of this permeability damage can be quantified, the oil saturation degree corresponding to each pressure point cannot be measured. To address this, the relationship between condensate-containing oil saturation and gas phase permeability damage rate was established. Using the steady-state method and the principle of conservation of matter, a correlation curve between the gas phase permeability of rock samples and the saturation of condensate-containing oil was obtained. This relationship allowed

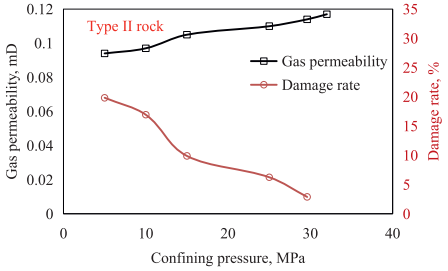


Fig. 19. The retrograde condensation damage of Sample T103-1(9/67).

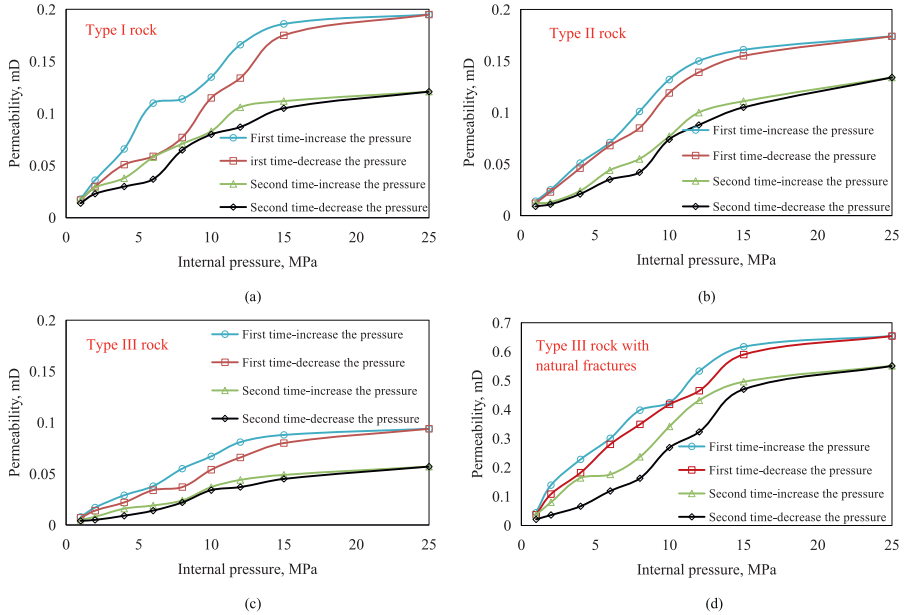


Fig. 18. Permeability change rate after two cycles of increasing and reducing internal pressure. (a)Sample T105-1(47/54); (b) Sample T104-3(47/63); (c) Sample T101-1(18/53); (d) Sample T110-2(54/55).

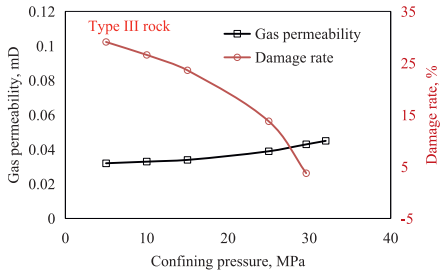


Fig. 20. The retrograde condensation damage of Sample T103-1(9/67).

for the inference of oil saturation levels following condensate oil contamination, based on measured gas phase permeability (Fig. 21). The results indicate that gas phase permeability decreases sharply as the initial oil saturation increases. The initial gas phase permeability values correspond to a condensate oil saturation range of 2.15%–3.24%. The greater the rock permeability, the smaller the resulting damage rate when condensate oil contamination occurs.

4.6. Condensate oil pollution control methods

4.6.1. Wetting inversion method

The super-amphiphobic nano-displacement agent injected into the formation comes into contact with the bound oil, which substantially reduces the oil's interfacial tension. This tension reduction causes the oil to detach and peel off from the rock or bound water surfaces, thereby allowing it to flow and significantly increasing the rock's permeability. For instance, injecting the agent into sample T103-1 (16/67) increased its gas phase permeability from 0.00372 mD under bound water conditions to 0.0207 mD. This represents a gas phase permeability recovery of 77.2% (Table 4).

4.6.2. Re-evaporation of condensate oil

When the pressure in the core drops to 5 MPa, inject nitrogen until the initial pressure reaches 32 MPa. Allow the core to stand for 12 h before testing the nitrogen permeability. After this soaking period, the effective gas phase permeability of the core rose from 0.046 mD to 0.0537 mD (Table 5). This increase suggests that using gas injection, followed by well shut-in (soaking), to restore near-wellbore pressure improves energy efficiency and mitigates anti-condensate pollution.

In addition to the wetting inversion method and re-evaporation of condensate oil, retrograde condensation and water lock damage can generally be mitigated through a combination of production optimization techniques, specifically optimizing the mining system, implementing water-controlled fracturing, and performing reservoir transformation. For optimizing the mining system, the production pressure difference can be adjusted; it can be reduced to control water invasion or increased to enhance gas liquid-carrying capacity. The overall mining system can be optimized to appropriately increase the recovery rate. Water-controlled fracturing can improve the physical properties of the reservoir, reduce the degree of water locking, and connect gas seepage channels, which can significantly increase the recovery.

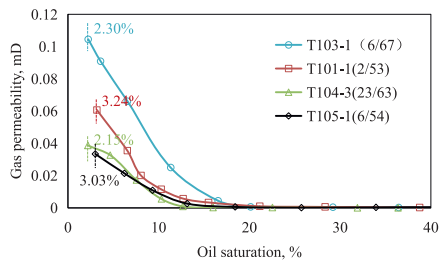


Fig. 21. Gas phase permeability of rocks under different oil saturation conditions.

5. Discussion

The reservoir in the Sichuan Basin is experiencing a rapid decline in production, and this could be attributed to two reasons. First is poor physical properties; the rock has low permeability due to small pore radii and poor connectivity. Second is water damage; the gradual water encroachment into the gas-producing layer causes severe damage from retrograde condensation and water locking. To maintain or increase stable output, in addition to the wetting inversion method, re-evaporation of condensed oil, optimized mining system, water control fracturing, and other methods discussed above, a comprehensive water control strategy needs to be formulated. This strategy is generally summarized by three phases: early waterproofing, mid-term water control, and late-stage water control. In the early stage (waterproofing and prevention), the focus is on preventing early water production and extending the water-free gas production period. This is achieved by deepening the understanding of fluid distribution and employing numerical simulation technology to predict development outcomes based on different well types, well patterns, production allocations, and production rates. In the mid-term stage, the goal is to manage existing water encroachment, suppress the non-uniform advancement of water fronts, and reduce the harm caused by uneven water invasion. This is achieved by dynamically predicting water invasion, optimizing single-well production allocation, improving the development well network, and optimizing drainage gas production technology. In the last stage, due to insufficient formation energy, the focus shifts to maximizing remaining reserves. Here, fine gas reservoir description technology is utilized to accurately track the pattern of water invasion and the distribution of remaining reserves. Through the optimization of water control plans, drainage processes, and wellhead pressurization, we can alleviate the impact of water seals and water locks, reduce the abandonment pressure of gas reservoirs, maximize the use of remaining reserves, and improve the overall gas reservoir recovery rate.

Reasonable well layout and effective drainage gas production are the basic requirements for a successful water control strategy. Effective gas reservoir water control technology hinges on three key strategies: paying close attention to the impacts of linkage, strict adherence to regulatory rules/guidelines, and proactive capitalization on opportunities. High-quality, comprehensive production dynamic monitoring is essential to ensure the expected results are guaranteed. This requires establishing a dynamic monitoring well network in a timely manner, strengthening monitoring efforts (focusing on pressure, fluid, and production logging), and carrying out effective dynamic analysis and quantitative forecasting of water intrusion patterns to provide a scientific basis for governance decisions and measures. Furthermore, implementing an integrated water control approach requires continuous adjustment and dynamic optimization across five key areas: (1) Dynamic optimization of water control methods such as waterproofing, water control, and drainage based on the specific development stage and water invasion conditions of the gas reservoir. (2) Dynamic optimization of the timing of interventions based on the stage and degree of water invasion, such as before water production begins, after initial signs appear, or after

Table 4
Comparison of permeability before and after injection of a super-amphiphobic nano-displacement agent.

Gas permeability (mD)	0.0268
Gas permeability under bound oil conditions (mD)	0.0037
Gas permeability after injection of super amphiphobic nano-displacement agent (mD)	0.0207
Gas permeability recovery (%)	77.2

Table 5
Permeability changes in the T104-1(44/53) rock sample during condensate oil reverse evaporation method.

Pressure (MPa)		Gas velocity (ml/min)	Pressure difference (MPa)	Permeability (mD)
Retrograde condensation phase of pressure failure	32	38.51	0.12	0.058
	29.6	34.63	0.08	0.056
	25	37.25	0.14	0.054
	15	31.92	0.08	0.052
	12	30.41	0.09	0.048
	5	30.19	0.11	0.046
Pressure retention recovery	5	36.36	0.13	0.054

significant water breakthrough. (3) Dynamic optimization of strategies for different well types according to their specific needs and characteristics, such as water-producing wells, water-flooded wells, and water-zone wells. (4) Dynamic optimization of the scales of gas production, drainage, and reinjection according to the requirements for achieving a balanced water control scale. (5) Dynamic optimization of water control technology using mature, efficient, and new technology trials tailored to specific well needs. Establish an integrated management model for drainage gas production to address water problems scientifically and efficiently and to increase overall gas field production: “Liquid loading assessment - liquid accumulation volume measurement - drainage process optimization - process effect analysis - process system optimization - overall process evaluation.”

6. Conclusions

The analysis of the tight sandstone reservoirs involved a multifaceted approach to comprehensively understand their characteristics and fluid flow mechanisms. The pore-throat characteristics were investigated using cast thin sections, NMR, and micro-CT techniques. Next, the fluid seepage characteristics were analyzed through pressure sensitivity tests, threshold pressure measurements, relative permeability experiments, and condensate oil contamination assessments. By combining the results from numerical simulation and these physical experiments, the study provided a comprehensive and in-depth understanding of the pore characteristics and seepage mechanisms within the tight sandstones. Furthermore, digital core technology was employed to analyze the relationship between pore structure and fluid seepage characteristics. This study offers valuable insights for researchers investigating similar tight sandstone reservoirs. It also helps oil and gas developers optimize their production strategies and enhance well stimulation measures.

The main types of pores observed within the reservoir rock were residual primary intergranular pores, intergranular dissolution pores, intragranular dissolution pores, mold pores, and occasional mixed base pores and microcracks. The effective porosity of the reservoir was 7.56%–12.39%. It exhibited low permeability of 0.135–6.09 mD, with an average permeability value of 0.388 mD. The reservoir was mainly composed of nanometer-to 10-μm-sized micropores. The pore size distribution varied by reservoir type; Type I and Type II reservoirs exhibited a multi-peak characteristic and were highly sensitive to stress changes and condensate oil contamination, while Type III reservoirs had a smaller, single-peak pore size distribution.

During cycles of increasing and decreasing confining and internal pressures, the permeability testing showed a strong recovery hysteresis. The rock exhibited strong stress sensitivity to confining pressure, but weak sensitivity to internal pressure. Water-gas flow tests showed a co-permeability range of 41.43%–56.13% and high irreducible water saturation at 32%–41%. The average gas phase damage rate in the irreducible water state was 64%. The reservoir flow exhibited a required starting pressure gradient, which was approximately 0.0014–0.00189 MPa/cm for the Type II reservoirs and 0.00255–0.00344 MPa/cm for Type III reservoirs.

After retrograde condensation occurs, the resulting condensate oil is trapped within the rock pore throats, significantly reducing gas phase permeability. The average damage rate is 24.7%, corresponding to the condensate oil saturation of 2.3%–7.5%. Gas field operators can mitigate this damage and manage water issues through several strategies. These include optimizing the mining system and operational methods, injecting wettability reversal agents to alter the rock's surface properties, supplement formation energy through condensate reverse evaporation, and transform reservoirs using water-controlled fracturing techniques. A comprehensive, life-cycle water control strategy—that is, early waterproofing, mid-term water management, and late-stage control—is essential for stabilizing and increase gas field production. Establish an integrated management model for drainage gas production to address water problems scientifically and efficiently and increase overall gas field production: “Liquid loading assessment - liquid accumulation volume measurement - drainage process optimization - process effect analysis - process system optimization - overall process evaluation.”

CRediT authorship contribution statement

Jia Kang: Writing – original draft, Software, Resources, Methodology, Formal analysis, Data curation, Conceptualization. **Gang Liu:** Software, Methodology, Formal analysis, Conceptualization. **Xin Kang:** Writing – original draft, Software, Methodology, Investigation, Formal analysis. **Peng Hu:** Software, Formal analysis, Methodology, Resources. **Licai Qu:** Writing – review & editing, Resources, Project administration, Methodology, Data curation, Conceptualization.

Declaration of competing interest

The authors declare that they have no competing financial interests or personal relation-ships that could have appeared to influence the work reported in this paper.

References

Ajagbe, O., Fahes, M., 2020. Establishing screening criteria for field application of wettability alteration in gas-condensate reservoirs. J. Petrol. Sci. Eng. 195, 107342. https://doi.org/10.1016/j.petrol.2020.107342.

Behrang, A., Mohammadmoradi, P., Taheri, S., Kantzas, A., 2016. A theoretical study on the permeability of tight media; effects of slippage and condensation. Fuel 181, 610–617. https://doi.org/10.1016/j.fuel.2016.05.048.

Gao, J.B., Sun, N.L., Hao, B., 2025. Lithologic characteristics and reservoir evolution of tight sandstones in the upper Triassic Xujiahe formation, northeast Sichuan basin, China. Unconvent. Res. 6, 100162. https://doi.org/10.1016/j.uncres.2025.100162.

Huang, M., Wu, L.H., Su, D.C., Zhao, Z.R., Zhang, M.X., 2023. Enhancing gas production in low-permeability natural gas hydrate reservoirs by the axial water jet slotting and grouting in vertical wellbores. Gas Sci. Eng. 118, 205088. https://doi.org/10.1016/j.jgsce.2023.205088.

Huang, Y.T., Li, Y.M., Liu, F.J., Chang, C., Xie, W.Y., 2022. Key technologies and progress of enhanced gas recovery in water-bearin carbonate gas reservoirs. Nat. Gas. Ind. B 9, 336–346. https://doi.org/10.1016/j.ngib.2022.07.003.

Jiang, L., Zhao, W., Bo, D.W., 2023. Tight sandstone gas accumulation mechanisms and sweet spot prediction, Triassic Xujiahe formation, Sichuan basin, China. Pet. Sci. 20, 3301–3310. https://doi.org/10.1016/j.petsci.2023.07.008.

Kalam, Z., Gibrata, M., Hammadi, M.A., Mock, A., Lopez, O., 2019. Validation of digital rock physics based water-oil capillary pressure and saturation exponents in super giant carbonate reservoirs. In: SPE Middle East Oil and Gas Show and Conference. https://doi.org/10.2118/164413-MS.

Kamel, K.E.M., Gerard, P., Colliat, J.B., Massart, T.J., 2022. Modelling stress-induced permeability alterations in sandstones using CT scan-based representations of the pore space morphology. Int. J. Rock Mech. Min. Sci. 150, 104998. https://doi.org/10.1016/j.ijrmms.2021.104998.

Kang, J., Li, N.Y., Zhao, L.Q., 2022. Construction of complex digital rock physics based on full convolution network. Pet. Sci. 19 (2), 651–662. https://doi.org/10.1016/j.petsci.2021.11.018.

Kang, J., He, Y.J., Lu, H., 2023. Study on the diverting characteristics of diverting acid based on digital rock physics. Energy Fuel. 37, 15006–15024. https://doi.org/10.1021/acs.energyfuels.3c02574.

Li, W.P., 2022. Low permeability reservoir water locking damage factors and preventive measures. Fine Spec. Chem. 30 (9), 27–29. https://doi.org/10.19482/j.cn11-3237.2022.09.07 (in Chinese).

Liu, K., Zhu, W.Y., Pan, B., 2023a. Laboratory evaluation on oil-soluble resin as selective water shut-off agent in water control fracturing for low-permeability hydrocarbon reservoirs with bottom aquifer. Geoenergy Sci. Eng. 225, 211672. https://doi.org/10.1016/j.geoen.2023.211672.

Liu, X.Q., Ma, L.T., Liu, C., Ge, Y., Xiong, J.J., Liu, D.K., 2023b. Pore scale water locking mechanism and concentration optimization of drainage aids in tight sandstone gas reservoirs. Petrochem. Indust. Appl. 42 (1), 65–70. https://doi.org/10.3969/j.issn.1673-5285.2023.01.014 (in Chinese).

Mohamadi-Baghmolaei, M., Sakhaei, Z., Azin, R., Osfouri, S., Zendehboudi, S., Shiri, H., Duan, X., 2021. Modeling of well productivity enhancement in a gas-condensate reservoir through wettability alteration: a comparison between smart optimization strategies. J. Nat. Gas Sci. Eng. 94, 104059. https://doi.org/10.1016/j.jngse.2021.104059.

Sadegh, K., Asra, F., Martin, B., Saenger, E.H., 2019. Computing heterogeneous core sample velocity using digital rock physics: a multiscale approach. Comput. Geosci. 135, 104378. https://doi.org/10.1016/j.cageo.2019.104378.

Tran, K., Odike, B., Garcez, J., Ayala, L., 2024. Improved saturation-pressure relationship and multiphase pseudo-pressure calculations for retrograde gas reservoir production under boundary-dominated flow. Gas Sci. Eng. 125 (5), 205289. https://doi.org/10.1016/j.jgsce.2024.205289.

Zahedizadeh, P., Osfouri, S., Azin, R., 2022. Accurate, cost-effective strategy for lean gas condensate sampling, characterization, and phase equilibria study. J. Petrol. Sci. Eng. 210, 110085. https://doi.org/10.1016/j.petrol.2021.110085.

Zhang, A.G., Fan, Z.F., Zhao, L., 2020. An investigation on phase behaviors and displacement mechanisms of gas injection in gas condensate reservoir. Fuel 268, 117373. https://doi.org/10.1016/j.fuel.2020.117373.

Zhang, Y.F., Long, A.F., Zhao, Y., Zang, A., Wang, C., 2023. Mutual impact of true triaxial stress,borehole orientation and bedding inclination on laboratory hydraulic fracturing of Lushan shale. J. Rock Mech. Geotech. Eng. 15 (12), 3131–3147. https://doi.org/10.1016/j.jrmge.2023.02.015.

Zhang, Y.F., Long, A.F., Zang, A.N., Zhao, Y., 2025. Pore-scale damage evolution in sandstone induced by fluid infiltration under various stress conditions. Int. J. Rock Mech. Min. Sci. 193, 106181. https://doi.org/10.1016/j.ijrmms.2025.106181.

Zhao, L.Y., Liu, X.Y., Zhang, L.H., Tang, H.M., Xiong, Y., Guo, J., Shan, B.C., 2021. Laws of gas and water flow and mechanism of reservoir drying in tight sandstone gas reservoirs. Nat. Gas. Ind. B 2 (8), 195–204. https://doi.org/10.1016/j.ngib.2020.09.018.